Microstructure evolution and elevated temperature wear performance of in-situ laser-synthesized Ti-25Al-17Nb coating on Ti-6Al-4V

Wensheng Li [a, b, *], Winbin Zhang [a,d], Haimin Zhai [b, *], Shuncai Wang [c], Qiang Song [a], Robert J.K. Wood [c] , Qijing Sun [a] , Bo cheng [b], Dongqing He [b]

a. School of Materials Science and Engineering, Shandong University of Science and Technology, Qingdao 266590, Shandong, China

b. State Key Laboratory of Advanced Processing and Recycling of Non-ferrous Metal, Lanzhou University of Technology, Lanzhou, 730050, Gansu, China

c. National Centre for Advanced Tribology, Faculty of Engineering and the Environment, University of Southampton, Southampton SO17 1BJ, United Kingdom

d. Northwest Aluminum Corporation Limited, Aluminum Corporation of China, Longxi, 748100, Gansu, China

Abstract

A ternary Ti-25Al-17Nb coating was fabricated from the pre-alloyed powder by in-situ laser synthesis. The powder was laser scanned to form α_2 phase at high temperature and subsequently precipitated O phase in an acicular structure following the rapid Ar gas cooling. The O phase continuously grows to form a lamellar structure with α_2 phase. The layered O phase has enough growth accommodation and is not deformed during the solidification growth process. In contrast, the secondary fine acicular O phase was squeezed due to the expansion of the α_2 phase with induced some edge dislocations and mixed dislocations. The phase distribution of coating is dominantly O phase (about 89.5 vol. %) and a few α_2 phase (about 4.3 vol. %). When the coating is subjected to a dry sliding wear test at 800°C, due to the good high-temperature oxidation resistance and good high-temperature toughness of O phase, the coating exhibited excellent wear resistance. The dense and hard Al_2O_3 film gradually replaced the loose and porous TiO_2 oxide film as an oxygen diffusion barrier, thereby reducing the possibility of brittle oxide formation in the coating and significantly increasing the wear resistance and oxidation resistance of the coating at 800°C.

***Key words*:** O-based alloys; Ti-25Al-17Nb coating; Laser in-situ synthesis; Microstructure; high temperature wear performance

1. Introduction

Compared with traditional Ti_3Al based alloys, orthorhombic Ti_2AlNb-based alloys (O-based alloys) have excellent high-temperature strength, oxidation and creep resistance. Therefore, it is often used as a metallic structural material in the aviation and aerospace [1-3]. In 1988, Banerjee et al. [4] first discovered the O phase in Ti-Al-Nb ternary alloys determined it as an orthogonal structure and had a specific orientation relationship with the parent phase (Ti_3Al phase, α_2). The addition of Nb stimulated the nucleation of the O phase, which significantly improved the strength, toughness and creep resistance of the α_2 phase.

Generally, the Ti_2AlNb-based alloys have three phases at room temperature: bcc phase (B2), hcp phase (α_2, D_019 structure based on Ti_3Al) and orthorhombic phase (O, Cmcm system based on Ti_2AlNb) [5, 6]. The phases interaction have a significant impact on their mechanical properties. Kamat et al. [7] found that the B2 phase passivated the microcrack growth in Ti-24Al-15Nb alloys. The B2 phase has two types slip systems {110} <1-11> and {112} <11-1> in which the latter is prone to twin deformation in {112} <11-1> [8], hence the B2 phase with ordered structure often endures plastic deformation to improve fracture toughness. The α_2 phase with the close-packed hexagonal structure is small in size and mainly distributed in the grain boundaries [9], which inhibits the growth of B2 phase and plays a role in grain refinement. The twinning deformation rarely occurs in the hcp structure and only the {0001} <11-20> slip system can slide. The α_2 phase is therefore usually regarded as a strengthening phase in the O-based alloys [10]. The O phase has the basic structure as α_2 except the lattice constants of the O phase expanded by 2.91% in the X-axis, and shrunk by 2.72% in the Y-axis [11]. Similar to the α_2 phase, the O phase can undergo twinning deformation behavior in the (110), (001), (221) plane [12]. Nevertheless, the O and α_2 phases usually possess a specific orientation relationship in O-based alloys [11]. In addition, the coarse O phase with content greater than 40% will increase ductility and reduce strength, while the needle-shaped O phase will increase the strengthening and decrease the toughness. Recently, Zhang et al. [13] reported that the fine lamellar O phase in the O-based alloys has good fatigue fracture resistance under various strain amplitudes, largely due to the slippage of the plastic zone dislocations before the crack tip. The O-based alloys have relatively good ductility which is crucial for the formation of fatigue striation.

It is generally recognized that a dense oxide film can effectively prevent surface oxidation even at high temperatures. The oxidation products of O-based alloys may include the TiO_2, Al_2O_3, $AlNbO_4$, and perhaps Nb_2O_5 phases. In the high-temperature atmosphere, the TiO_2 and Al_2O_3 oxide film will simultaneously form on the surface of O-based alloys. However, these symbiotic oxide films have different roles: the dense structure of Al_2O_3 oxide film will form a barrier for self-protection and oxidation resistance [14], while the intrinsic porous structure of rutile TiO_2 promotes the oxidation process. The $AlNbO_4$ oxide layer is formed on the surface of O-based alloys and generated oxygen diffusion channels, leading to the formation of dense oxide films and reducing the self-repairing ability of oxidation [15]. Researchers have proposed many technologies that inhibit the growth of TiO_2 and promote the formation of a protective layer of Al_2O_3 to enhance the oxidation resistance of O-based alloys. For instance, adjusting the content of Nb element or adding Si, Zr and Mo elements [14, 16-18]. Among them, Nb can effectively improve the activity of Al element and reduce the concentration of oxygen vacancies in the TiO_2 lattice by hindering the diffusion of Ti and oxygen. However, the addition of Nb has a range of limitations [17, 19].

Excessive Nb will form $AlNbO_4$ and Nb_2O_5 at high temperatures, and the formation of an ordered intermetallic phase (Nb_2Al) reduces the oxidation resistance of O-based alloys [20]. Therefore, the Nb content in O-based alloys is usually maintained at 21~27 at. %. The orthorhombic Ti2AlNb-based alloy with high Nb content has been proven to possess extremely excellent oxidation resistance at high temperature to 800~900℃ [21], so it is considered a lightweight high-temperature structural material with great potential to replace Ti_3Al alloy.

In summary, O-based alloys have good high-temperature strength, creep properties, and oxidation resistance. They can provide long-life wear and oxidation resistance if they are coated on the base material for service in a high-temperature environment. At the same time, laser in-situ synthesis cladding is to apply powder metallurgy to additive manufacturing technology. Due to its simple synthesis process, low dilution rate, good combination, purity and compactness, laser in-situ cladding has been widely used in coating preparation [22-25]. In this work, the Ti-25Al-17Nb (the third generation O-based alloy) powder was synthesized by laser in-situ on the surface of Ti-6Al-4V alloy to prepare a Ti-Al-Nb intermetallic coating. The structural evolution during the solidification process of the coating was investigated in detail. In addition, the prepared O-based alloy coating was also tested at elevated temperatures of 25℃, 200℃, 400℃, 600℃, 800℃. The results show that the Ti-25Al-17Nb alloy coating has high temperature wear resistance at 800℃, which can improve the high-temperature oxidation resistance and wear resistance of Ti-6Al-4V alloy. It is also expected to provide a reference for applying O-based intermetallic coating synthesized by laser in situ synthesis in a high-temperature oxidation environment.

2. Experimental

2.1. Sample preparation

The Ti-6Al-4V substrate (Al: 5.0%-6.5%, V: 3.5%-4.5%, Fe: 0.186%, Si: 0.019%, O: 0.05% and balance Ti, wt. %) was machined into plate with a size of 100 mm × 100 mm × 10 mm followed by sandpaper polish to remove the oxide film. The Ti (50-74 μm), Al (74-150 μm) and Nb (~45 μm) raw material powders with a purity greater than 99 wt.% were mixed in the ratio of Ti-25Al-17Nb (at. %). The mixed powders were bonded on the surface of the substrate with polyvinyl alcohol to form a coating with a thickness of about 1 mm. Finally, the sample was placed in an environment over 120℃ to dry for 4 hours.

The fiber laser cladding with a maximum output power of 4 kW (IPG, YLS-4000, λ=1.07 μm) was employed in the in-situ synthesis of Ti-25Al-17Nb coating. The optimized processing parameters are listed in Table 1. The distance between the laser nozzle and Ti-6Al-4V substrate was set to 5 mm. Ar gas was used to cool and protect the molten pool from oxidization using the flow rate of 10 L min^{-1}. The cladding process is shown in Fig. 1 with the laser scanning overlap rate of about 30%

Table 1 Experimental parameters of laser cladding.

Powders	Output power	Scanning speed	Defocus amount	Laser beam diameter	Preplaced thickness	Energy density
Ti-25Al-17Nb	1.4 kW	10 mm s^{-1}	+15 mm	3 mm	1 mm	46.7 J mm $^{-2}$

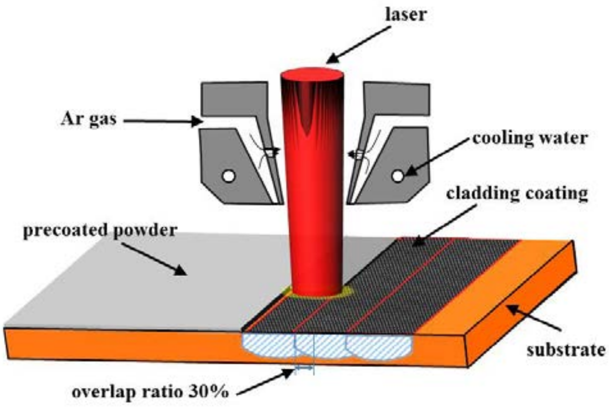

Fig. 1 Schematic of the laser cladding process

2.2 Microstructure characterization

The coating after laser cladding was cut, inlaid with resin, polished and chemical etched with 5 ml HF+5 ml HNO_3+90 ml H_2O solution for 10-15 s. The phase structure of the coating was characterized by the X-ray diffractometer (XRD, D8 Discover, Bruker, Cu-Kα radiation) with 2θ diffraction angles ranging from 30° to 90° at a step size of 0.02 °/s. The microstructure and element distribution of coating were investigated by the field emission scanning electron microscope (SEM, Quanta450 FEG) with energy-dispersive spectroscopy (EDS, AztecX-Max80). The detailed microstructure of the coating was carried out by transmission electron microscope (TEM, JEM-2010F). The surface layer of coating was cut into thin slices (20 mm × 20 mm × 1 mm) and then mechanically polished to 40 μm with SiC sandpaper. The thin foils for TEM observation were perforated by twin-jet electro-polishing in 5% perchloric acid, 35% butanol and 60% methanol solution at −70 °C. The crystallographic orientation of the coating was analyzed by electron backscatter diffraction (EBSD, HKL Nordly, Oxford) with an accelerating voltage of 20 KV, and a step size of 0.5 μm. The EBSD samples were also electropolished with 5% perchloric acid, 35% butanol and 60% methanol solution at −30 °C. The hardness of coating was measured by a Vickers microhardness meter (HV-1000) at a load of 500 g and a duration time of 10 s.

2.3 High temperature wear test

The high-temperature dry sliding wear tests of the coating (ϕ 18.5×5 mm) were performed at Ball-on-disk unidirectional tester (HT-1000, ZhongKeKaiHua Corporation, China).) at 25℃, 200℃, 400℃, 600℃ and 800℃. The applied load, sliding speed, sliding time are 5 N, 10 mm s^{-1}, 30 mins, respectively. The SiC ball with a diameter of 6 mm and a hardness of 1300 Hv was selected as the counterpart. The wear tracks and wear volume were investigated by a probe-type measurement tester (MT500, ZhongKeKaiHua Corporation, China). The wear rate W was calculated using $W=VF^{-1}L^{-1}$, where V is the wear volume, F and L are the applied load (N) and the corresponding sliding distance (m), respectively. To ensure the reliability of the data, the friction performance experiment under each friction condition was repeated 3 times to get the average value. Furthermore, the wear scars, corresponding cross-section and debris were characterized by SEM and EDS.

3. Results and discussion

3.1. Structure characterization of laser cladding Ti-25Al-17Nb coating

Fig. 2(a)-(c) show the microstructure morphology of coating, the coating has a compact, non-porous and uniform microstructure of the average thickness about 530 μm. From the BSE image in Fig. 2(b), different lengths lamellar phase distributed in the coating, and there is no obvious contrast difference between the lamellar phase and the matrix, indicating that the difference in composition between the two is not significant. The high magnified SE image in Fig. 2(c) shows some irregularly distributed needle-like phases in the area surrounded by lamellar phases. Fig. 2(d) shows the XRD analysis result of laser cladding Ti-25Al-17Nb coating surface, indicating that the appearance of the Ti_2AlNb (O) phase and Ti_3Al (α_2) phase. Fig. 2(e) shows the longitudinal section Vickers hardness distribution of the coating. The hardness of the coating is above 460 $Hv_{0.5}$.

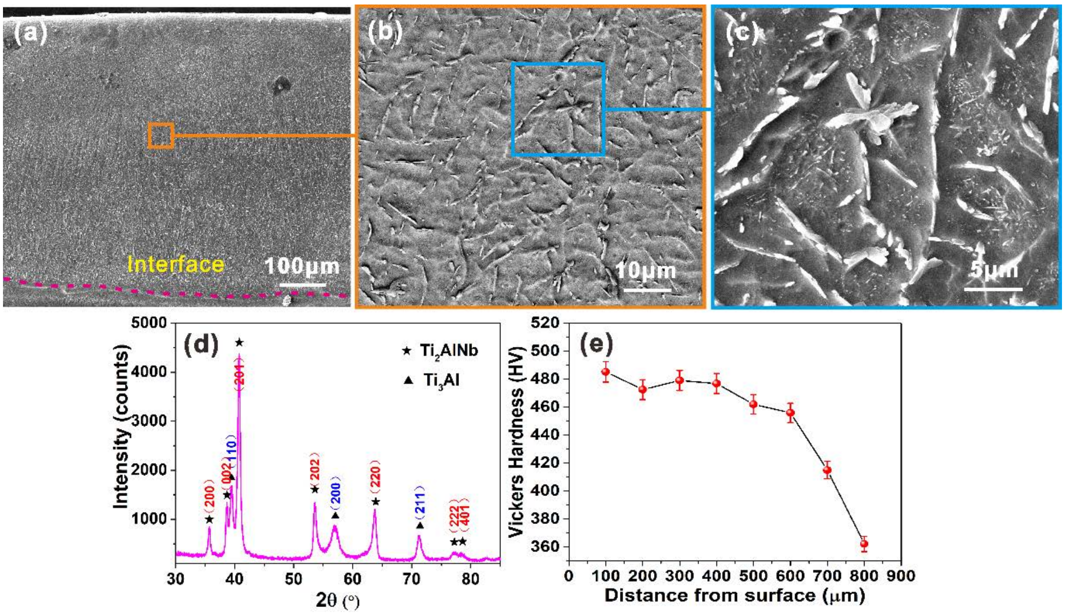

Fig. 2 The laser in-situ cladding Ti-25Al-17Nb coating: (a) SE image at low magnification; (b) BSE image; (c) SE image at high magnification, (d) XRD pattern; (e) Cross-sectional hardness against distance from the surface of the coating

Fig. 3 shows the near-surface EBSD pattern of the coating. Similar to Fig. 2(c), there are many black needle-like structures inside the coating, as shown in Fig. 3(a). The phase distribution of coating shows that it is basically composed of O phase (about 89.5 vol. %). A few α_2 phase (about 4.3 vol. %) appears in some grains and the edges of grain boundaries, as shown in Fig. 3(b). Both the layered and needle-like structures are O phase, and the former is the first precipitate O phase and the needle-like structure is the second precipitate O phase. The orientation distribution in Fig. 3(c) shows the varied grain size. the orientation difference between small grains is relatively large, but between the large grains is small, suggesting that a largish deformation occurred inside small grains. In addition, there are some acicular phases with different orientations inside the crystal grains. Combining Fig. 2(c) and Fig. 3(a), it can be concluded that these acicular phases are O phases. From the crystallization map in Fig. 3(d), the recrystallized and deformed structures are mainly distributed in small crystal grains, while the substructures mainly appear in large crystal grains, indicating that in the small crystal grain area, the recrystallized structure occurs due to the uneven local heat distribution. From the stress distribution map in Fig. 3(e), it can be found that the stress is mainly concentrated in the vicinity of small grains and grain boundaries, indicating that the heavy deformation between small grains causes stress concentration and more distinguishable misorientation angle distribution.

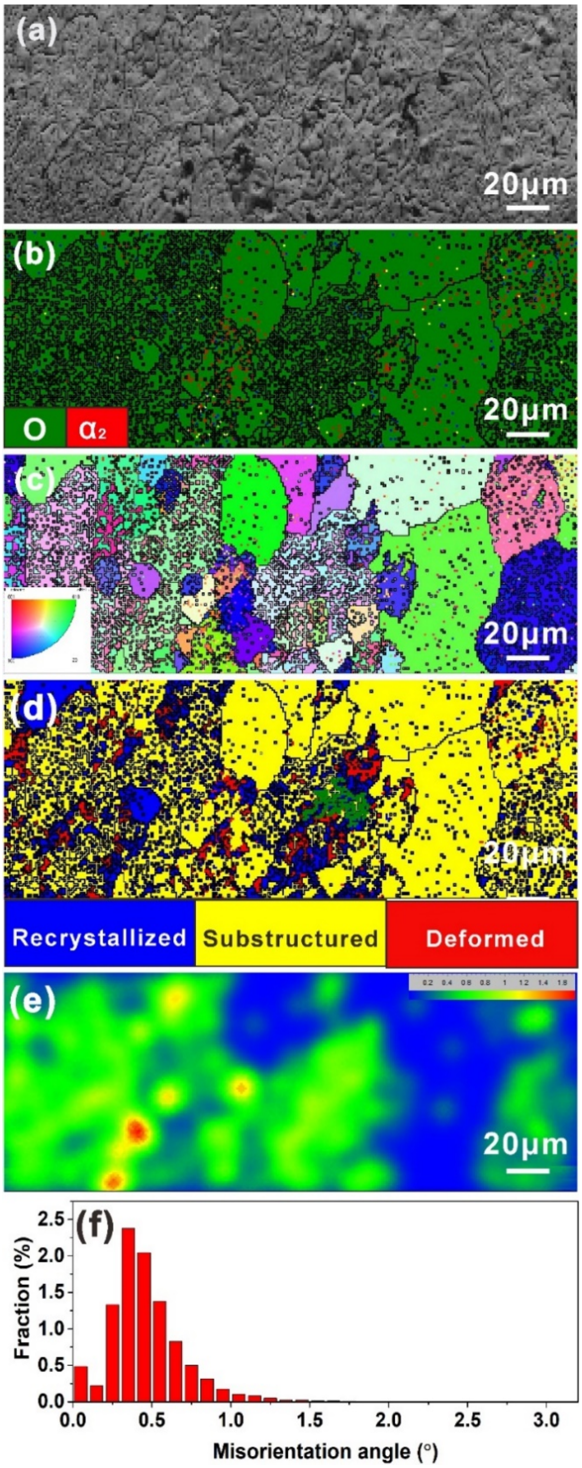

Fig. 3 The near surface EBSD pattern of laser cladding Ti-25Al-17Nb coating: (a) BSE image; (b) phases map; (c) orientation map; (d) crystallization map; (e) stress distribution map;(f) misorientation angle

Fig. 4 shows the bright-field TEM images and the corresponding selected area electron diffraction (SAED) pattern. The coating is mainly composed of thick lamellar and needle-like phases interlaced with each other in random directions. In addition, a small amount of black phase is distributed in the boundary between the lamellar phase and the acicular phase. The SAED pattern can be indexed as α_2 phase, as shown in Fig. 4(a). Similar to the morphology in Fig. 2(b) and (c), the layer with a length of several to ten microns and a width of several tens to hundreds of nanometers was observed. The SAED mode analysis inferred that this layered phase should be the first precipitate O phase, as shown in Fig. 4(b). Fig. 4(c) shows that the finer α_2 phase is embedded in the layered O phase and overlaps each other, which satisfies a specific orientation relationship, namely (001) O // (0001) α_2 [4, 11, 26]. The clear interface between the acicular O phase and the α_2 phase matrix indicates that the acicular O phase is a substructure existed in the α_2 phase grains, as shown in Fig. 4(e) and Fig. 4(f).

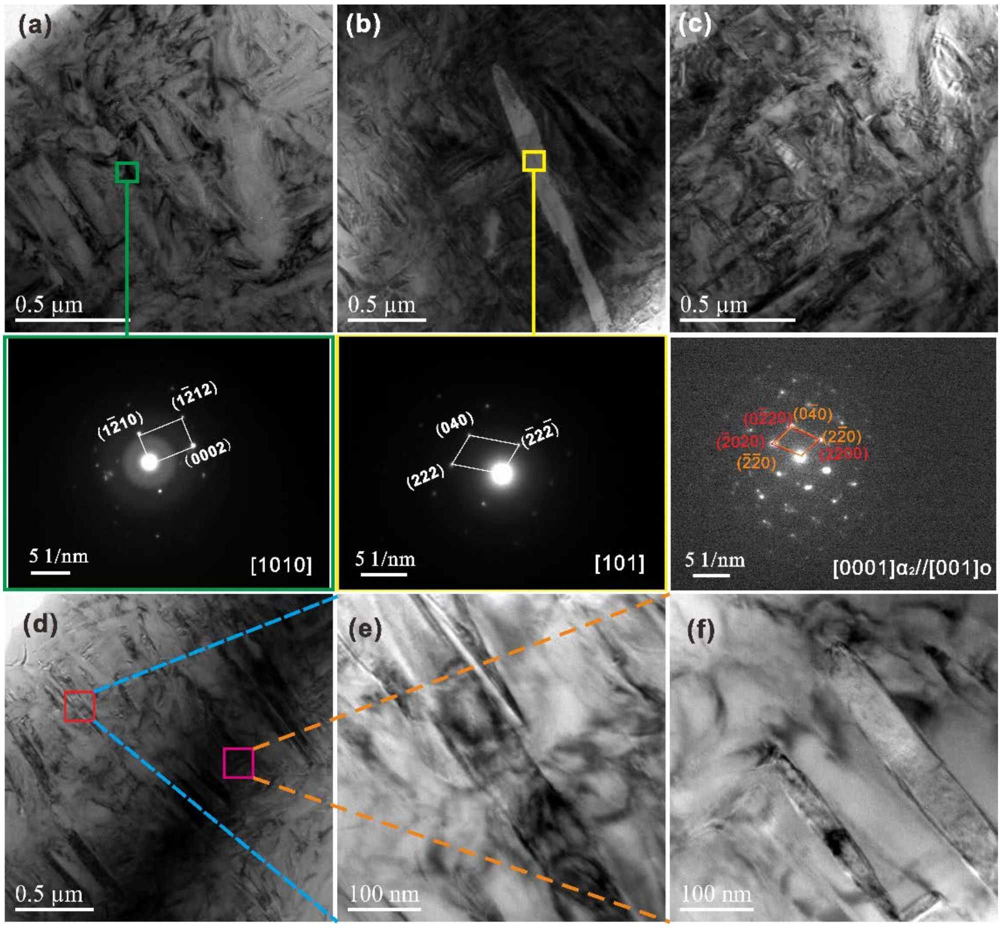

Fig. 4 Bright-field TEM micrographs and the corresponding SAED pattern in the laser cladding Ti-25Al-17Nb coating: (a) coexistence of α_2 phase and O phase; (b) coexistence of large lamellar O phase and acicular O phase; (c) overlapping of lamellar O phase and α_2 phase; (d) coexistence of lamellar O phase and acicular O phase; (e)-(f) high magnification micrograph of the corresponding area in Fig. 4(d)

Fig. 5 shows the high-resolution TEM (HRTEM) micrograph and the corresponding inverse fast Fourier transform (IFFT) image. During the laser cladding process with Ar gas cooling, the coating undergoes rapid solidification, and there are a large number of sub-crystals inside the O phase grains, as shown in Fig. 5(a). The local IFFT pattern shows that there are apparent semi-coherent and incoherent lattices inside the O phase grains, indicating that noticeable lattice distortion and imperfect dislocation slip behavior have occurred, that is, the O phase grains have suffered severe plastic deformation, as shown in Fig. 5(b). Fig. 5(c) and (d) show the HRTEM photos of the coarse lamellar O phase and the corresponding IFFT pattern. The orientation of the coarse lamellar O phase is the same, and there is no obvious lattice distortion, which indicates that the internal structure of the coarse lamellar O phase has a small degree of plastic deformation. According to the IFFT pattern analysis results in Fig. 5(e), (f) and (g), the black area should be the α_2 phase. Due to their different diameters and interaction forces, the Al, Ti, and Nb atoms occupy individual positions of the regular hexagon to form this specific phase, as shown in Fig. 5(f) [4]. In addition, the IFFT pattern of the black area in Fig. 5(g) shows the local lattice in the α_2 phase of mirror-symmetrical, indicating that the local twinning behavior occurs in the α_2 phase. Combining Fig. 3(b), the distribution of α_2 phase in O phase was relatively low, and majority were formed at the grain boundaries of O phase. The formation and evolution mechanism of phases in the in-situ laser cladding Ti-25Al-17Nb coating will be discussed in detail in section 3.2.

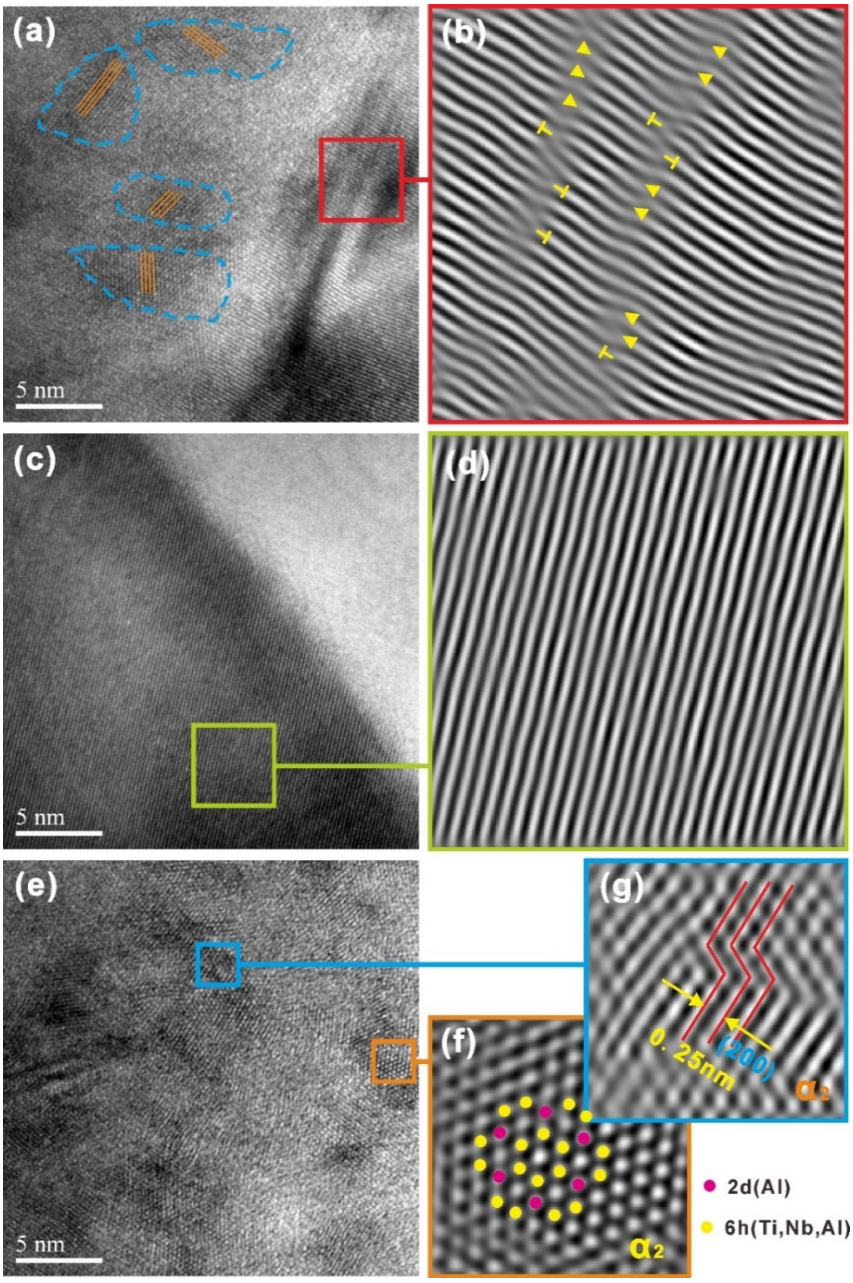

Fig. 5 (a) HRTEM images (a, c, e) and the corresponding IFFT pattern (b, d, f, g) of the O phase and α_2 phase inside of the laser cladding Ti-25Al-17Nb coating ("⊥" stands for edge dislocation, "▲" stands for lattice distortion)

3.2 Microstructure evolution in the in-situ laser cladding Ti-25Al-17Nb coating

In the in-situ laser cladding process, the Ti-25Al-17Nb mixed powders were melted by a high-density laser scanning under the protection of Ar gas which cools down quickly to form a solid coating. From Fig. 2(a), there were only Ti_2AlNb (O) and Ti_3Al (α_2) phases existed at room temperature. HRTEM images in Fig. 5 show that the internal direction of the crystal lattice is different at equal intervals, indicating that the structure has undergone severe deformation during the rapid solidification process, which leads to sub-crystals in some grains. Fig. 3(b) shows that the α_2 phase only exists in a small part of the grains of the entire coating, and the α_2 phase has apparent twinning (Fig. 5(e)). In general, the α_2 phase is difficult to deform in which twinning occurs only under severe deformation [10]. This may be due to the precipitation of O phase from the α_2 phase during the solidification process by Ar gas cooling, which leads to partial volume strain, thereby increasing the lattice constant [6, 27, 28]. According to the calculation results of Bendersky et al. [29], Pathak et al. [6], and Ren et al. [26], the O phase usually has lower free energy at relatively low temperatures (600°C) than that of the α_2 phase in Ti-Al alloys with high Nb content (5-20 at. %), hence the O phase is more stable at relatively low temperatures. Moreover, Rackel et al. [28] studied the phase transition behavior of Ti-Al alloys by using the HEXRD and DSC, and also found that in the range of 500-700°C, the O phase is easy to precipitate from the α_2 phase.

During the rapid solidification process of Ti-25Al-17Nb coating in-situ laser synthesized, the α_2 phase was first precipitated from the liquid phase due to its stable state at high temperature. As the temperature decreases, the stable O phase is continuously precipitated from the α_2 phase, as schematically described in Fig. 6(a). The deformation of the nascent first precipitate layered O phase is kept minimum as the lattice direction and spacing of the nascent first precipitate layered O phase are same, as shown in Figs. 4(b), 5(c) and 5(d). In addition, the grain orientation difference of the coating is between 0.5° (Fig. 3(f)), indicating that the orientation difference between the O phases formed during the solidification process is fairly small, and no serious plastic deformation occurs. In the Ti-Al-Nb ternary alloy with $Ti_{72.5}Al_{27.5}Nb_x$, the O phase alloy has a wider phase interval [30], therefore, more layered O phases will continue to grow as shown in Fig. 6(b) and (c). However, during subsequent solidification, the growth of the secondary O phase is restricted within the nascent first precipitate layered O phase. This also causes the second precipitate O phase to form a needle-like grain of hundreds of nanometers at a comparative higher cooling rate. Therefore, once the first precipitate O phase starts to precipitate from the α_2 parent phase, the volume of the local area will expand, and the remaining α_2 phase is squeezed to cause twinning deformation [31] as shown in Fig. 5(e). In addition, the SAED analysis proved that the α_2 phase and the nascent first precipitate O phase lattice satisfy the specific orientation relationship, namely $(001)O//(0001)\alpha_2$ [4, 11, 26]. It indicates that the phase transition behavior from α_2 phase to O phase occurred during the cooling process of the coating. Consequently, the local O phase is severely distorted in the form of sub-grains. This is also the main reason for the different orientations of the O-phase sub-grains in Fig. 5(a). Due to the extremely high cooling rate of the laser in-situ synthesis process, the α_2 phase precipitated in the coating does not have enough time to transform during the subsequent cooling process completely, and a small amount of the α_2 phase remains inside the newly formed O phase or near the grain boundary, as shown in Fig. 3(b). Hence, the Ti-25Al-17Nb coating synthesized in situ by laser on the Ti-6Al-4V substrate finally forms a two-phase structure of the O phase (about 89.5 vol. %) and α_2 phase (about 4.3 vol. %) at room temperature, as shown in Fig. 6(d).

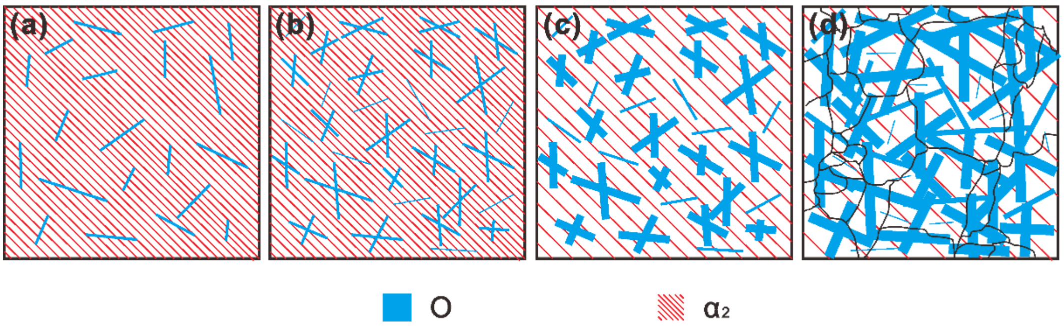

Fig. 6 Schematic illustration of morphological evolution of the O phase and α2 phase

3.3 Dry sliding wear behavior of the Ti-25Al-17Nb coating at elevated temperatures

Fig. 7 shows the friction coefficient curves and wear rates of the in-situ laser cladding Ti-25Al-17Nb coating at 25℃, 200℃, 400℃, 600℃, and 800℃. The coating has a relatively high coefficient of friction (COF) of 0.91 at room temperature (25℃). In the range of 25~400℃, with the increase of temperature, the COF decreases to 0.57 at 400℃. As the temperature increased continually to 600℃, the COF increased to 0.79, and dropped to 0.68 when the temperature increased to 800℃. The changing trend of wear rate is similar to the change of COF, as shown in Fig. 7(b). The wear rates in the range of 25~400℃ show a continuous downward trend. When the temperature is 600℃, the wear rate increases significantly to 9.286×10^{-3} mm^3/Nm, and the wear rate is significantly reduced by order of magnitude to 3.91×10^{-4} mm^3/Nm at 800 °C. The above results all show that the current laser cladding Ti-25Al-17Nb coating has good wear resistance and friction reduction performance at 800 °C. This could be mainly due to the existence of a large number of O phases with excellent high-temperature oxidation resistance in the coating.

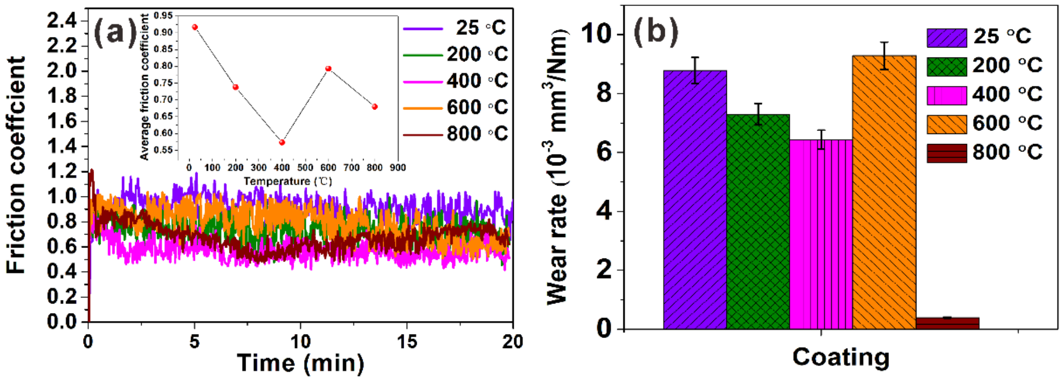

Fig. 7 In-situ laser cladding Ti-25Al-17Nb coating at different temperatures: (a) COF curves, (b) wear rate

Fig. 8 shows the two-dimensional profile topography of the cross-section and morphologies of wear scars, the debris and SiC ball friction counterpart after worn at 25℃, 200℃, 400℃, 600℃, and 800℃. At the range of 25~400 °C, the plastic deformation areas and spalling pits appear on the coating worn surface (Fig. 8(a3)-(c3)), and locally with severe plastic deformation peeled off, curled and large flaky wear debris, as shown in Fig. 8(a4). As the temperature increases, the sectional area of wear scar on the coating surface is significantly reduced (Fig. 8(a1)-(c1) and Fig. 8(a2)-(c2)). The thickness and quantity of the wear debris show a gradual decrease, as shown in Fig. 8(a4)-(c4). Correspondingly, as the wear tests temperature increases, the adhesion wear on the SiC counterpart's surface gradually increases (Fig. 8(a6)-(c6)), and the size of the wear scar appears to decrease as a whole, as shown in Fig. 8(a5)-(c5). A similar phenomenon is shown in Fig. 3(b) where the secondary-level acicular O phase in the coating has a local enrichment. Due to the severe plastic deformation during its formation (Fig. 4(b), the secondary-level acicular O phase tends to cause the coating brittleness. Once the applied shear force is greater than the yield strength of the coating, cracks will develop in the coating. Moreover, there is inevitably air in the cracks in the atmospheric environment, which will be forced to compress under the repeated rolling of periodic contact stress and force the cracks to expand inside the coating [32]. When the cracks in the coating expand to a certain extent, they will form a cantilever state, break at the root of the soft cantilever, and finally form laminar wear debris. However, with the increase of the test environment temperatures, the stress in the secondary-level acicular O phase of the coating is gradually released, and the brittleness of the coating is gradually reduced. Because the O phase content in the coating is as high as 89.5 vol. %, especially the first precipitate O phase content exceeds 2/3, the coarse first precipitate layered O phase can effectively increase the toughness of the coating. As the temperature increases [11], the wear rate of the coating shows a gradually decreasing trend.

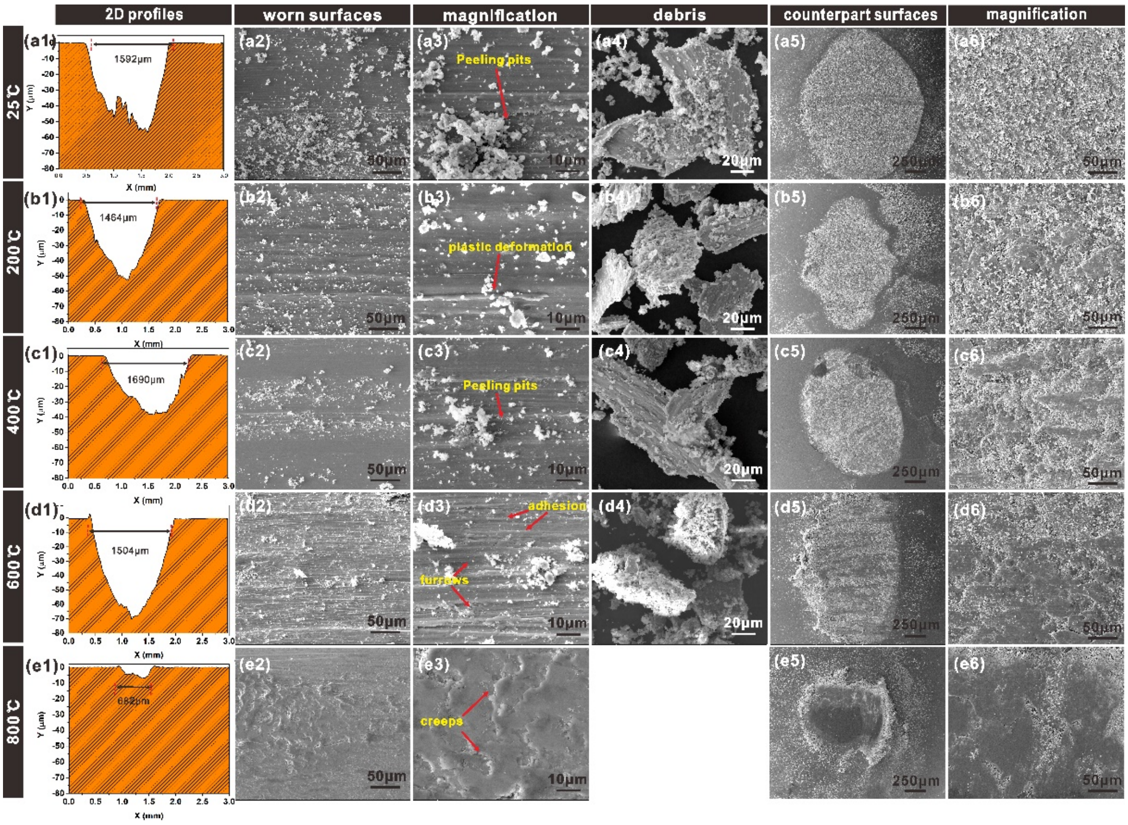

Fig. 8 Two-dimensional (2D) profiles, wear morphologies, wear tracks magnification and debris morphologies of the coating and the corresponding wear scar morphologies and magnification images of the SiC ball counterpart at different temperatures: (a1)-(a6) 25 ℃; (b1)-(b6) 200 ℃; (c1)-(c6) 400 ℃; (d1)-(d6) 600 ℃; (e1)-(e6) 800 ℃

On the other hand, the abrasion test in the atmospheric environment will inevitably promote the gradual increase of the O content in the coating, which shows good high-temperature lubricity by forming a TiO_2 film layer. As the test temperature increases, the content of the TiO_2 lubricating film formed on the wear scar of coating surface will increase with COF reduction from 0.91 (25°C) to 0.57 (400°C). Due to the effect of the TiO_2 lubricating film, the contact area between the coating and the SiC counterpart gradually decreases, which significantly reduces the thickness and number of lamellar wear debris as shown in Fig. 8(a4)-(c4). As a result, the amount of wear debris involved in wear is greatly reduced, and even no lamellar wear debris could be collected at 800°C, which significantly reduces the COF and wear rate of the coating (Fig. 7).

When the wear test temperature rises to 600 °C, the depth and sectional area of the wear scar increases again (Fig. 8(d1)-(d2)), evidenced by deep furrows on the worn surface (Fig. 8(d3)) and debris after severe plastic deformation adhered to the furrow. This may be due to the decrease in the critical shear strength of the coating peeling off under the action of regular fatigue wear at the test temperature of 600 °C, causing large strips of peeling debris on the coating surface and deep furrows. It can be observed that wear debris changes from lamellar (400°C) to irregular block shape, and fatigue wear was induced [32]. The SiC counterpart will contact different depths of furrows during dry sliding wear, making the sliding extremely unstable, so the COF of the coating at 600°C fluctuates severely, and the average friction coefficient rises to 0.79 again (Fig. 7(a)). Moreover, as the test environment temperature reaches 600°C, more TiO_2 films are formed on the surface of the coating. As we mentioned in the introduction, TiO_2 films are inherently loose and porous [15]. Therefore, a large number of TiO_2 films formed on the surface of the coating will be more likely to break and peel off, which will lead to a significant increase in the COF and wear rate of the coating at 600°C. Furthermore, it can be found from Fig. 9 that at 600°C, the concentration of Ti and O elements on the surface of the SiC friction counterpart increases, which also indicates that the TiO_2 film on the coating surface has peeled off and adhered to the SiC friction counterpart surface.

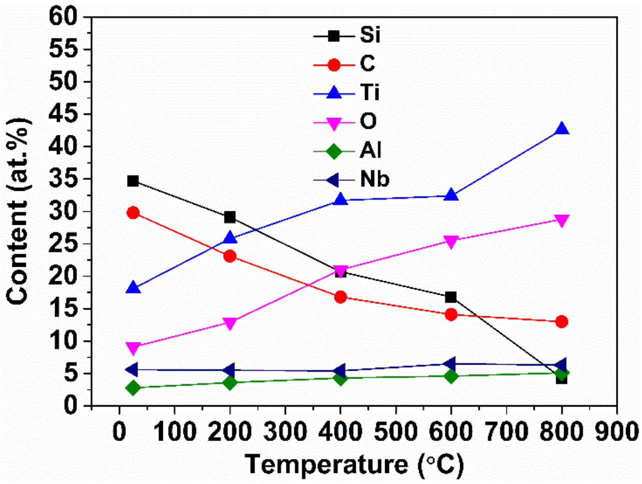

Fig. 9 Curve of surface composition change of the SiC ball counterpart at different temperatures

When the wear test temperature rises to 800 °C, the width of the coating wear scar area is significantly reduced. There is apparent plastic deformation, and no significant wear debris is observed (Fig. 8(e1)-(e3)), which indicates that the coating has softened significantly. Due to the softening of the coating, a significant adhesion behavior occurred between the SiC friction counterpart and the coating, causing a large amount of Ti and O elements on the coating surface to adhere to the wear surface of the SiC friction counterpart, as shown in Fig. 9. This is also consistent with the situation at 600°C. In addition, the content of Al element increases to adhere on the surface of SiC which indicates that Al_2O_3 oxide film is formed and increased with the temperature increases. The denser and harder Al_2O_3 oxide film gradually replaces the loose and porous TiO_2 film. It effectively inhibits the brittle fracture of the oxide film on the coating surface, so the COF and wear rate of the coating at 800°C are again significantly reduced. On the other hand, with an effective oxygen diffusion barrier, the thick Al_2O_3 oxide film at high temperatures will prevent Ti from further oxidation and brittle TiO_2 in the form of loose porous oxide film.

4 Conclusions

In this work, under the cooling and protection of argon gas, a Ti_2AlNb coating was successfully prepared on the surface of the Ti-6Al-4V substrate according to the atom ratio of Ti-25Al-17Nb by laser in-situ synthesis method. The microstructure evolutions of the Ti_2AlNb (O) phase and Ti_3Al (α_2) phase were investigated by SEM, EBSD and HRTEM. The wear performance of the laser in-situ cladding Ti_2AlNb coating in the evaluation of temperature was also studied. The main conclusions are as follows:

(1) The Ti, Al, and Nb powders are quickly heated to a liquid state by laser scanning, and these powders react with each other to form α_2 phase at high temperatures. The O phase continuously precipitated from α_2 phase. The Ti-25Al-17Nb coating structure is mainly composed of O phase (89.5 vol. %) and α_2 phase (4.3 vol. %). The content of α_2 phase at the grain boundary is relatively high, and the α_2 phase also hinders the growth of second precipitate O phase grains, resulting in a relatively small grain size of 1.0-1.5 μm in the deformed region. The first precipitated O phase continuously grows to form a lamellar structure, and the later precipitated O phase forms an acicular structure due to the rapid cooling of the coating.

(2) In the late stage of solidification, the second precipitate O phase can only grow in the framework formed by the primary O phase, where the growth space is restricted and cause edge dislocations and mixed dislocations. During the phase transformation, the volume of the local area expands, and the residual α_2 phase is squeezed to cause twinning deformation.

(3) At 25~400 °C, the coating undergoes fatigue peeling wear under the regular contact stress. The peeled wear debris participates in the friction process to form three-body wear. With the increase of temperature, the wear debris particles are reduced, and the wear rate gradually decreases. At 600 °C, the formation of loose porous oxide TiO_2 film makes the coating surface more prone to brittle. The reduced critical shear strength for coating peeling makes the coating much deeper furrows and severe wear.

(4) At 800 °C, the dense and hardened Al_2O_3 oxide film gradually replaces the loose and porous TiO_2 oxide film, hindering the diffusion of oxygen into the coating and reducing the possibility of brittle oxide formation. With the increase of the dense Al_2O_3 film of good lubricity, the COF and wear rate of the coating are therefore significantly reduced.

Acknowledgments

The work is supported by National Natural Science Foundation of China (52075234， 51901092), Major Special Projects of Gansu Province (21ZD4WA017)， University Industry Transformation Promotion Project of Gansu (2020C-11), and the program of Science and Technology International Cooperation Demonstrative Base of Metal Surface Engineering along the Silk Road (2017D01003) and the “111” project (D21032).

Declaration of interest statement

The authors declare that they have no known competing financial interests or personal relationships that could have appeared to influence the work reported in this paper.

References

[1] J. Bresler, S. Neumeier, M. Ziener, F. Pyczak, M. Göken, Mater. Sci. Eng. A 744 (2019) 46-53.
[2] S. Suwas, R.K. Ray, Mater. Sci. Eng. A 391 (2005) 249-255.
[3] L. Song, L.Q. Zhang, X.J. Xu, J. Sun, J.P. Lin, Scripta Mater. 68 (2013) 929-932.
[4] D. Banerjee, A.K. Gogia, T.K. Nandi, V.A. Joshi, Acta Metall. 36 (1988) 871-882.
[5] J. Jia, W. Liu, Y. Xu, C. Lu, H. Liu, Y. Gu, J. Luo, Mater. Sci. Eng. A 730 (2018) 106-118.
[6] A. Pathak, A.K. Singh, Solid State Commun. 204 (2015) 9-15.
[7] S.V. Kamat, A.K. Gogia, D. Banerjee, Acta Mater. 46 (1998) 239-251.
[8] T.O. Erinosho, A.C.F. Cocks, F.P.E. Dunne, Int. J. Plasticity 50 (2013) 170-192.
[9] H. Inui, Y. Toda, M. Yamaguchi, Philos. Mag. A 67 (1993) 1315-1332.
[10] L. Song, L. Wang, M. Oehring, X. Hu, F. Appel, U. Lorenz, F. Pyczak, T. Zhang, Intermetallics 109 (2019) 91-96.
[11] G. Ren, J. Sun, Acta Mater. 144 (2018) 516-523.
[12] N. V. Kazantseva, S. L. Demakov, A. A. Popov, Phys. Met. Metallogr. 103 (2007) 378-387.
[13] Y. Zhang, A. Feng, S. Qu, J. Shen, D. Chen, J. Mater. Sci. Technol. 44 (2020) 140-147.
[14] Y. Pan, X. Lu, M.D. Hayat, F. Yang, C.C. Liu, Y. Li, X.Y. Li, W. Xu, X.H. Qu, P. Cao, Corros. Sci. 166 (2020) 108449.
[15] Q.W. M. Guo, P. Ke, Y. Cui, J. Gong, C. Sun, L. Wen, Acta Metall. Sin. 41 (2005) 312-316.
[16] J. Dai, H. Zhang, C. Sun, S. Li, C. Chen, Y. Yang, Corros. Sci. 168 (2020). 108578.
[17] J. Zheng, X. Hou, X. Wang, Y. Meng, X. Zheng, L. Zheng, Corros. Sci. 96 (2015) 186-195.
[18] C. Ciszak, I. Abdallah, I. Popa, J.-M. Brossard, A. Vande Put, D. Monceau, S. Chevalier, Corros. Sci. 172 (2020) 108611.
[19] J. Dai, N. Zhang, A. Wang, H. Zhang, C. Chen, J. Alloy. Comp. 765 (2018) 46-57.
[20] J.P. Lin, L.L. Zhao, G.Y. Li, L.Q. Zhang, X.P. Song, F. Ye, G.L. Chen, Intermetallics 19 (2011) 131-136.
[21] M. Yoshihara, K. Miura, Intermetallics 3 (1995) 357-363.
[22] W. Zhang, W. Li, H. Zhai, Y. Wu, S. Wang, G. Liang, R.J.K. Wood, Sur. Coat. Tech. 395 (2020) 125944.
[23] A. Grigoriev, I. Polozov, V. Sufiiarov, A. Popovich, J. Alloy. Comp. 704 (2017) 434-442.
[24] C.T. Kwok, ninth ed., Woodhead Publishing, cambridge, 2012.
[25] Y.P. Kathuria, Sur. Coat. Tech. 132 (2000) 262-269.
[26] G. Ren, C. Dai, W. Mei, J. Sun, S. Lu, L. Vitos, Acta Mater. 165 (2019) 215-227.
[27] H. Gabrisch, U. Lorenz, F. Pyczak, M. Rackel, A. Stark, Acta Mater. 135 (2017) 304-313.
[28] M.W. Rackel, A. Stark, H. Gabrisch, N. Schell, A. Schreyer, F. Pyczak, Acta Mater. 121 (2016) 343-351.
[29] L.A. Bendersky, W.J. Boettinger, Acta Metall. Mater. 42 (1994) 2337-2352.
[30] V.T. Witusiewicz, A.A. Bondar, U. Hecht, T.Y. Velikanova, J. Alloy. Comp. 472 (2009) 133-161.
[31] Q. Cai, M. Li, Y. Zhang, Y. Liu, Z. Ma, C. Li, H. Li, Mater. Charact. 145 (2018) 413-422.
[32] Z-P Zhao, P-F Xu, H-X Cheng, X-Y Lu, C Cheng, Wear 428–429 (2019) 217–222.